Honeycomb-lattice plasmonic absorbers at NIR: anomalous high-order resonance

Yiting Chen,[1] **Jin Dai,**[1] **Min Yan,**[1] **and Min Qiu**[2,1*]

[1]*Optics and Photonics, School of Information and Communication Technology Royal Institute of Technology (KTH), Kista 16440, Sweden*
[2] *State Key Laboratory of Modern Optical Instrumentation and Institute of Advanced Nanophotonics, Department of Optical Engineering, Zhejiang University, Hangzhou 310027, China*

[*]*min@kth.se*

Abstract: We design, fabricate and characterize a plasmonic honeycomb lattice absorber with almost perfect absorption at 1140 nm over a wide incident angle range. This absorber also possesses a narrow-band, angle- and polarization-dependent high-order resonance in the short-wavelength range, with a bandwidth of 19 nm and angle sensitivity of 3 nm per degree. The nature of this high-order absorption band is analyzed through finite-element simulations. We believe it is due to Bragg coupling of the incident light to the backward-propagating surface plasmon polariton through the periodic modulation of the structure.Such fine absorption bands can find applications in plasmonic sensors and spectrally selective thermal emitters.

OCIS codes: (240.6680) Surface plasmons; (250.5403) Plasmonics; (220.3740) Lithography.

References and links

1. V. Shalaev, "Optical negative-index metamaterials," Nat. Photonics **1,** 41–48 (2007).
2. D. Smith, J. Pendry and M. Wiltshire, "Metamaterials and negative refractive index," Science **305,** 788 (2004).
3. J. Pendry, "Negative refraction makes a perfect lens," Phys. Rev. Lett. **85,** 3966–3969 (2000).
4. M. Yan, W. Yan, and M. Qiu, "Cylindrical superlens by a coordinate transformation," Phys. Rev. B **78,** 125113 (2008).
5. M. Yan, Z.C. Ruan, and M. Qiu, "Cylindrical invisibility cloak with simplified material parameters is inherently visible," Phys. Rev. Lett. **99,** 233901 (2007).
6. J. Gansel, M. Thiel, M. Rill, M. Decker, K. Bade, V. Saile, G. Freymann, S. Linden and M. Wegener,"Gold helix photonic metamaterial as broadband circular polarizer," Science **325,** 1513–1515 (2009).
7. N. Papasimakis, V. Fedotov and N. Zheludev , "Metamaterial analog of electromagnetically induced transparency," Phys. Rev. Lett. **101,** 253903 (2008).
8. Y. Ahn, J. Dunning, and J. Park, "Scanning photocurrent imaging and electronic band studies in silicon nanowire field effect transistors," Nano Lett. **5,** 1367 (2005).
9. O. Hayden, R. Agarwal, and C. Lieber, "Nanoscale avalanche photodiodes for highly sensitive and spatially resolved photon detection," Nat. Mater. **5,** 352 (2006).
10. P. Richards, "Bolometers for infrared and millimeter waves," J. Appl. Phys. **76,** 1 (1994).
11. M. Laroche, R. Carminati, and J. Greffet, "Near-field thermophotovoltaic energy conversion," J. Appl. Phys. **100,** 063704 (2006).
12. S. Lin, J. Moreno, and J. Fleming, "Three-dimensional photonic-crystal emitter for thermal photovoltaic power generation," Appl. Phys. Lett. **83,** 380 (2003).
13. J. Hao, J. Wang, X. Liu, W J. Padilla, L. Zhou, and M. Qiu, "High performance optical absorber based on a plasmonic metamaterial," Appl. Phys. Lett. **96,** 251104 (2010).
14. X. Liu, T. Starr, A. F. Starr, and W. J. Padilla, "Infrared Spatial and Frequency Selective Metamaterial with Near-Unity Absorbance," Phys. Rev. Lett. **104,** 207403 (2010).
15. J. Wang, Y. Chen, J. Hao, M. Yan, and M. Qiu, "Shape-dependent absorption characteristics of three-layered metamaterial absorbers at near-infrared," J. Appl. Phys. **109,** 074510 (2010).

16. C. Hu, Z. Zhao, X. Chen, and X. Luo, "Realizing near-perfect absorption at visible frequencies," Opt. Express **17,** 11039–11044 (2009).
17. A. Tittl, P. Mai, R. Taubert, D. Dregely, N. Liu, and H. Giessen, "Palladium-based plasmonic perfect absorber in the visible wavelength range and its application to hydrogen sensing," Nano Lett. **11,** 4366–4369 (2011).
18. M. Hedayati, M. Javaherirahim, B. Mozooni, R. Abdelaziz, A. Tavassolizadeh, V. Chakravadhanula, V. Zaporojtchenko, T. Strunkus, F. Faupel, and M. Elbahri, "Design of a perfect black absorber at visible frequencies using plasmonic metamaterials," Adv. Mater. **23,** 5410–5414 (2011).
19. D. Han, Y. Lai, J. Zi, Z. Zhang, and C. Chan, "Dirac spectra and edge states in honeycomb plasmonic lattices," Phys. Rev. Lett. **102,** 123904 (2009).
20. Y. Poo, R. Wu,Z. Lin, Y. Yang, and C. Chan, "Experimental realization of self-Guiding unidirectional electromagnetic edge states," Phys. Rev. Lett. **102,** 093903 (2011).
21. T.Kelf, Y. Sugawara, and J. Baumberg, "Plasmonic Band gaps and trapped plasmons on nanostructured metal surfaces," Phys. Rev. Lett. **95,** 116802 (2005).
22. T.Kelf, Y. Sugawara, R. Cole, and J. Baumberg, "Localized and delocalized plasmons in metallic nanovoids," Phys. Rev. B **74,** 245415 (2005).
23. M. Pu, C. Hu, M. Wang, C. Huang, Z. Zhao, C. Wang, Q. Feng, and X. Luo, "Design principles for infrared wide-angle perfect absorber based on plasmonic structure," Opt. Express. **19,** 17413–17420 (2011).
24. P. Johnson, and R. Christy, "Optical constants of the noble metals," Phys. Rev. B **6,** 4370-4379 (1972).
25. E. Palik, *Handbook of Optical Constants of Solids* (Academic, New York, 1985).

1. Introduction

Metamaterials (MMs) are artificially designed media with unique properties that are not obtainable in nature. Those properties origin from their structures rather than materials [1,2]. Due to their subwavelength unit size and exotic elctromagnetic properties, metamaterials can be designed for different applications such as perfect lens [3,4], cloaking devices [5], broadband circular polarizer [6] and electromagnetically induced transparency (EIT) devices [7]. Another important application of MMs is spectrally selective perfect absorber. Perfect absorbers can be employed as photodetectors [8,9], microbolometers [10] and thermal emittters for the thermalphotovoltaic applications [11, 12]. In recent years, there have been quite a lot of metamaterial absorbers realized experimentally in infrared [13–15] and visible [16–18] frequencies. In these papers, the strong absorption is achieved by utilizing the fundamental absorption peak, which is not sharp and only slightly angle-dependent. The engineered periodic nanostructure in those abosrbers is usually nanoparticles distributed in a square lattice or simple 1D metallic grating.

In this paper, we present a perfect metamaterial absorber consisting of a periodic array of gold nanoparticles with a honeycomb lattice. Similar to the structure of single-layer graphene, the plasmonic honeycomb lattice may have unique characters due to the vector nature of the plasmonic excitations [19,20], which is the reason why the absorber has a narrow-band, angle-sensitive high-order resonance, and this high-order resonance will be our focus in this work. For our sample, in addition to a strong absorption in fundamental mode, a prominent high-order absorption peak is also unveiled. Compared to the fundamental mode, this high-order resonance not only has a much narrower bandwidth, but also exhibits prominent redshift with respect to an increasing incident angle. The quality factor (Q_f) of the high-order resonance is about 7 times larger than that of the fundamental resonance. The differences between the fundamental mode and the red-shifting high-order mode come from their different nature: the former is localized plasmonic resonance and the latter is delocalized surface plasmon resonance [21–23]. As most papers mainly focus on the localized fundamental mode, our paper will not only experimentally demonstrate the red-shifting high-order mode, but also make more effort to study the nature and characteristics of the high-order mode. We believe the high-order mode with those unique features can be an alternative used for sensors and thermal emitters.

2. Design and experimental results

Our absorber is fabricated on a glass substrate. Firstly, the substrate is covered with 4 nm thick titanium, 80 nm thick gold and 28 nm thick alumina by electron-beam (E-beam) evaporation. The titanium layer works as an adhesion layer and also improves the surface smoothness of the gold film. While the thickness of the bottom layer is thick enough (80 nm) to reflect back most of the light and ensure more light wave is localized and absorbed. Then the positive resist Zep 520A is spinned onto the substrate and exposed by E-beam lithography. After development, the sample is deposited with 4 nm thick titanium and 30 nm thick gold. The honeycomb lattice absorber is finally realized after liftoff with acetone and remover 1165 in ultrasonic bath. As shown in Fig. 1(a), the schematic diagram of the metamaterial absorbor structure, the gold disk has a diameter of 180 nm and the distance between two closest disk center is 310 nm. The titanium layers are not shown in the schematic diagram. In Fig. 1(b), top-view scanning electron microscope (SEM) image of the abosrber is presented, with the inset SEM image with larger magnification ratio. From the SEM images, we can see that every particle possesses a reasonably good round shape and the absorber has an almost perfect honeycomb lattice.
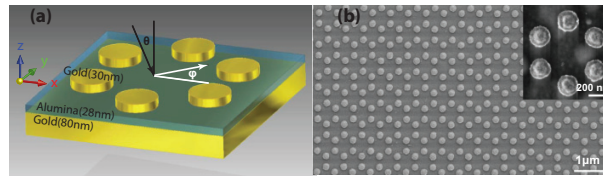

Fig. 1. (a) Schematic diagram of the structure of the honeycomb lattice metamaterial absorber. The bottom layer and nanodisks are gold and the middle layer is Al_2O_3. The inter-distance between two adjacent disks is 310 nm, and the diameter of the nanodisks is 180 nm. θ denotes the incident angle, and φ the sample azimuthal orientation. (b) Top-view SEM images of the absorber.

By means of our home-made angle-resolved transmission/reflection measurement setup [15], the wide-angle absorption spectra of the sample are measured with both polarizations and two different incident planes (plane xz and plane yz), as shown in Fig. 2. The absorption (A) spectra are simply obtained from measured reflection (R) results (i.e., A = 1 - R), because the transmission is negligible due to the 80 nm thick bottom gold film. For the case of electric field (E) perpendicular to the xz incident plane (S_{xz}), i.e., $E{\perp}S_{xz}$ (TE polarization), the sample has a 99% absorption around 1140 nm at normal incidence. As shown in Fig. 2(a), this absorption peak is not sensitive to the incident angle. It stays above 90% even when the incident angle increases up to 50° and drops to 86% at 60° incident angle. At both 50° and 60° incident angles, two small absorption peaks are found at 791 nm and 816 nm, with the absorption of 48% and 34% respectively. This angle-dependent high-order resonance may come from the coupling of fields between different gold disks, as it will be shown in the simulation results. In Fig. 2(b), for the case of magnetic field (H) perpendicular to the xz incident plane, i.e., $H{\perp} S_{xz}$, the sample also has perfect angle-independent absorption at 1140 nm, with the extinction of 99% at normal incidence and more than 97% absorption even up to 60° incident angle. More interestingly, a high-order absorption peak comes to exist in the short wavelength range (600 - 800 nm) at a larger incident angle. It first becomes distinct at 30° incident angle with the 35% absorption. As the incident angle increases, both its absorption strength and center wavelength increase. At 60° incident angle, the peak has moved to 787 nm with an absorbance of 70%. The resonant wavelength shifts from 671 nm to 787 nm as the incident angle varies from 20° to 60°, i.e., about 3 nm per degree. Besides, a third resonance appears at about 666 nm when the incident angle is equal to and larger than 40°.
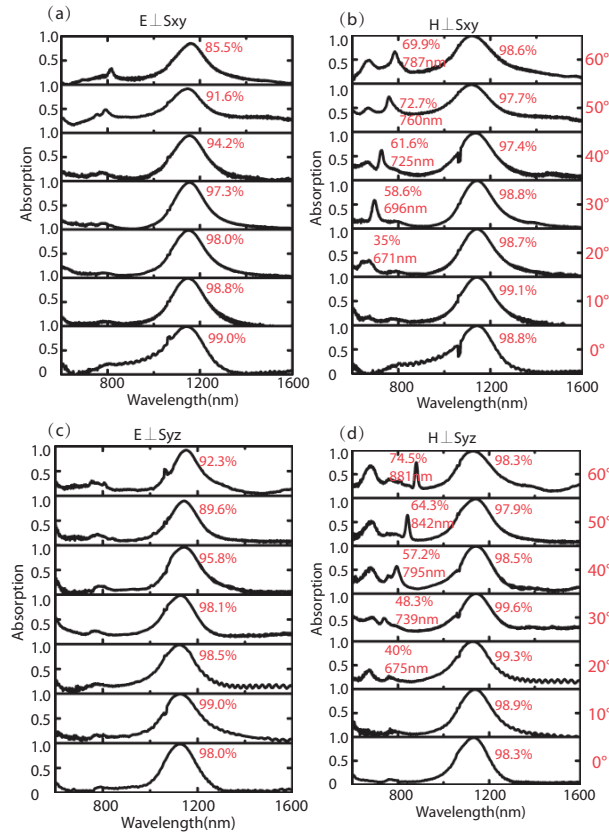
Fig. 2. Measured absorption spectra for both polarizations and orientations:(a) E⊥S$_{xz}$, (b) H⊥S$_{xz}$, (c) E⊥S$_{yz}$, (d) H⊥S$_{yz}$. Numbers 0° - 60° are corresponding to the incident angles. The maximum absorbance for each incident angle is also indicated in the figures.

Next, we investigated the absorption properties of the sample in the yz incident plane, which is achieved in experiment by rotating the sample by 90° in the xy plane. Again, absorption spectra of both polarizations (TE and TM polarizations) are obtained, which are shown in Fig. 2(c) and Fig. 2(d) respectively. For the case of electric field (E) perpendicular to the yz incident plane, i.e., E⊥S$_{yz}$ (TE mode), there is a 98% absorption at 1140 nm at normal incidence, and this peak remains above 89% even when the incident angle increases up to 60°. No red-shifting resonance appears at this polarization. For the case of magnetic field (H) perpendicular to the yz incident plane, i.e., H⊥ S$_{yz}$ (TM polarization), besides the strong absorption at 1140 nm, which decreases little with the increase of incident angle, there is also a red-shifting absorption peak in the short wavelength range. From 739 nm at 20° incident angle to 881 nm at 60° incident angle, this peak has a larger red-shifting ratio, almost 4 nm per degree. Compared to the fundamental resonance at 1140 nm, it also has very narrow bandwidth. For example, at 60° incident angle, the full width at half maximum (FWHM) of this high-order peak is only 19 nm. At 50°, it's 20 nm. With larger incident angle, a third peak becomes stronger at about 685 nm.

In summary, the sample has a fundamental resonance at 1140 nm, with perfect absorption over a wide range of incident angles for both polarizations. A narrow-band resonance can be found in the short wavelength range corresponding to large angle of incidence. This resonance not only exhibits a rapid red-shifting with regard to increasing incident angle, but also depends

on polarization: it does not appear for the $E\perp S_{yz}$ case, and it is much stronger in TM polarizations ($H\perp S_{xz}$ and $H\perp S_{yz}$).

3.   Simulations and Discussions
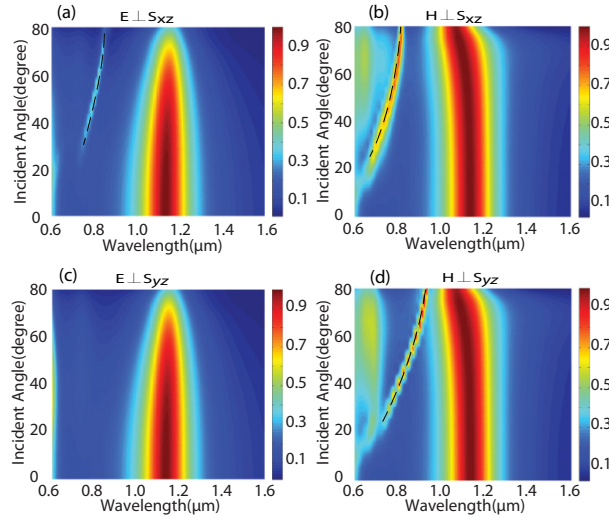

Fig. 3. Simulated absorption spectral map for both polarizations and orientations:(a) $E\perp S_{xz}$, (b) $H\perp S_{xz}$, (c) $E\perp S_{yz}$, (d) $H\perp S_{yz}$. The black dashed lines illustrate the angle-dependent high-order resonance.

To investigate the nature of such absorption and compare with the experimental results, we performed simulations on this structure with the same parameters as the fabricated sample. With the assistance of a 3D finite-element method based commercial software COMSOL MULTI-PHYSICS, we calculated the absorption spectra and field distributions, which are presented in Fig. 3 and Fig. 4 respectively. In the simulations, the dispersive permittivity of gold is taken from the data measured by Johnson and Christy [24], and those of titanium and alumina from Palik's book [25]. The simulation results of absorption spectra are in very good agreement with our experimental results. Firstly, for all four polarizations, there is a fundamental absorption peak at 1140 nm with almost perfect absorption (more than 99%), and this peak is not sensitive to the incident angle. Same as the experimental result, there is no red-shifting resonance only for the case of $E\perp S_{yz}$ polarization. For the case of $H\perp S_{yz}$ at 60° incident angle, the calculated red-shifting resonance has moved to 880 nm with the absorbance of 82% and bandwidth of 26 nm, very close to the experimental counterparts (74.5% and 19 nm at 881 nm).

To better understand the difference between the fundamental mode and red-shifting mode, we calculate the field distributions of both modes in the yz plane at x=0 nm [Fig. 4(a)]. Figure 4(b) gives the field distribution of the fundamental mode at 1140 nm at 0° incident angle for the case of $H\perp S_{yz}$ (TM polarization). We can see that the fundamental mode corresponds to a highly localized magnetic dipole resonance. With antiparallel currents circulating between the top layer gold particles and bottom gold film, the electromagnetic energy is confined in the intermediate dielectric layer effectively. There is almost no coupling between adjacent disks. Since the mode at 1140 nm is a single-particle resonance, the position of the resonance should not move even though the lattice is different. Indeed, we have also fabricated the same samples except with square or triangular lattices; and we have observed a very similar fundamental-mode resonance. While for the high-order resonance, as shown in Fig. 4(c), this resonance at
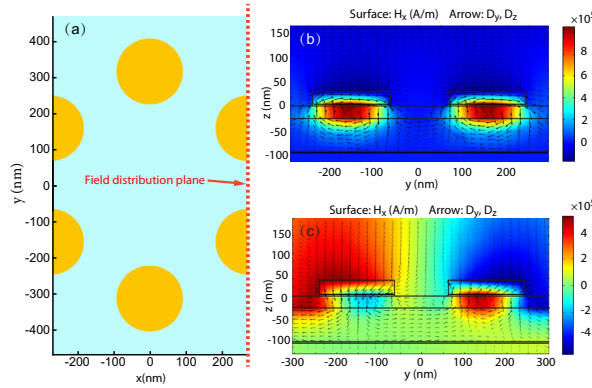
Fig. 4. (a) Schematic diagram of the structure in xy plane used in simulation. (b, c) Calculated field distribution in the yz plane at x=268.5 nm at resonances (b) at 1140 nm at normal incidence and (c) at 880 nm at $60°$ incident angle.

880 nm at $60°$ incident angle is clearly a Bloch mode (delocalized surface plasmon polariton (SPP)) [21–23]. Since it is a propagating mode, its field is extended along the surface-parallel direction, with its phase variation regulated by the mode's propagation constant β. Note that the presence of the top nanodisks slightly perturb the SPP's field distribution from its ideas case, i.e. without the nanodisks. According to paper [22], this delocalized Bragg mode is excited by the coupling of propagating wave with a reciprocal vector added to the in-plane wave vector $k_{\parallel}$ ($k_{\parallel} = k_0 \sin\theta$) of the wave, and it has a propagation constant which is equal to the surface-parallel component of the incidence's wave vector added by an integer number of reciprocal vectors of the periodic structure, or

$$\beta = \mathbf{k}_0 \cdot \sin\theta + \mathbf{q}_{mn},\tag{1}$$

where β is the propagating constant of the excited SPP, $\mathbf{k}_0$ is the wave vector of the incident light, and $\mathbf{q}_{mn}$ is the reciprocal lattice vectors. Since there is no $k_{\parallel}$ component at normal incidence, it explains why we can see the Bloch mode only at oblique incidence. According to both experimental and simulation results, this Bragg surface plasmon resonance moves towards longer wavelength when incident angle increases. The only possibility for this to happen is that the incident wave is coupled to a backward-propagating SPP mode guided by the periodic structure. To prove the argument, we present Fig. 5, where the absorption spectral for the $H \perp S_{yz}$ (TM polarization) case is shown in frequency-k_y space, and the dispersion relation of SPPs at an air/alumina/gold interface are given by red solid curves. The left red curve is for the backward-propagating SPP. In the color map in Fig. 5, the fundamental resonance is manifested as a flat band at frequency of 0.8 above the light line, and the red-shifting Bragg mode is represented by the downward moving band above the fundamental mode. We can see that the left red curve at $k_y = -1.5 \sim -1$ is very similar to the high-order mode at $k_y = 0.5 \sim 1$. If the left red curve is offset by 2 along k_y axis, as indicated by the black arrows, it may fit well with the high-order resonance. This offset is attributed to a reciprocal lattice vector $\mathbf{q}_{mn}$, which has the opposite direction against the incident wave. This proves that this high-order resonance is a backward propagating Bragg plasmon mode that propagates along the alumina/gold surface.

If we define the quality factor (Q_f) of the plasmonic resonance as the ratio of the resonance wavelength (λ_r) and the FWHM of the absorption peak:

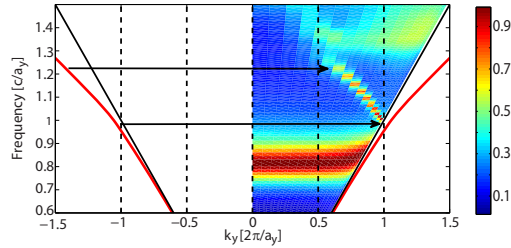$$Q_f = \frac{\lambda_r}{FWHM}\tag{2}$$

Fig. 5. Absorption spectral map shown in frequency-k_y for the TM mode in the yz incident plane. The light line of air is drawn in solid black line. Two red curves depict the dispersion relation of SPPs at an air/alumina/gold interface, with the left curve for the backward SPPs wave and the right curve for forward SPPs wave. The frequency is normalized by c/a_y, where c is the speed of light, and k_y is normalized by $2\pi/a_y$. a_y is 930 nm, the lattice constant along y-axis.

We will see that the Q_f of the high-order mode is much larger than that of the fundamental mode. For example, according to the simulation results, for the case of H$\perp$ S$_{yz}$ [Fig. 3(d)] at 60° incident angle, Q_f of the high-order resonance at 880 nm is 34 (the experimental result is even higher, reaching 46), while that of fundamental resonance at 1113 nm is 5.

4. Conclusion

In summary, we experimentally demonstrated a honeycomb-lattice metamaterial absorber, based on a metal-insulator-metal (MIM) structure, operating at the near-infrared regime. We performed the measurement of the absorption of the absorber at different incident angles for both polarizations and incident planes. It is found that besides almost perfect absorption for the fundamental mode (at 1140 nm), the absorber also possesses a narrow-band high-order resonance, which is a Bragg surface plasmon mode. This high-order resonance appears only at oblique incidence, and it has a red-shifting as the incident angle increases. The absorbance is also positively related to the incident angle. Besides, the bandwidth of the high-order mode is much narrower than the fundamental mode. Due to its narrow bandwidth and incident angle sensitive properties, this absorber has the potential to be utilized as high performance optical sensors and thermal emitters.